

SCIENTIFIC REPORTS

OPEN

Investigation on preparation and performance of spinel $\text{LiNi}_{0.5}\text{Mn}_{1.5}\text{O}_4$ with different microstructures for lithium-ion batteries

Received: 11 January 2015

Accepted: 20 July 2015

Published: 24 August 2015

Yuan Xue¹, Zhenbo Wang¹, Lili Zheng¹, Fuda Yu¹, Baosheng Liu¹, Yin Zhang¹ & Ke Ke^{1,2}

The high voltage spinel $\text{LiNi}_{0.5}\text{Mn}_{1.5}\text{O}_4$ is a promising cathode material in next generation of lithium ion batteries. In this study, $\text{LiNi}_{0.5}\text{Mn}_{1.5}\text{O}_4$ with various particle microstructures are prepared by controlling the microstructures of precursors. $\text{LiNi}_{0.5}\text{Mn}_{1.5}\text{O}_4$ spinel samples with solid, hollow and hierarchical microstructures are prepared with solid MnCO_3 , hollow MnO_2 and hierarchical Mn_2O_3 as precursor, respectively. The homemade spinel materials are investigated and the results show that the content of Mn^{3+} and impurity phase differ much in these three spinel samples obtained under the same calcining and annealing conditions. It is revealed for the first time that an inhomogeneous migration of atoms may introduce Mn^{3+} and impurity phase in the spinel. The hierarchical microstructure with the primary particles interconnected is optimal for electrode materials because this microstructure has a higher conductivity between the interconnected primary particles and appropriate specific surface area. $\text{LiNi}_{0.5}\text{Mn}_{1.5}\text{O}_4$ in this microstructure has the best rate capability and also the best long-term cycling stability.

With an escalating energy crisis and greenhouse gas emission issue, clean energy sources and electric vehicles (EVs) have increasingly attracted much attention. For an effective utilization of clean energy, efficient energy storage systems (ESSs) are indispensable. Among the well-developed ESSs, rechargeable lithium-ion batteries (LIBs) dominate in portable devices such as cell phones, laptops and etc. and are expected to dominate EVs in the near future. In the application of LIBs in EVs, however, it remains a challenge to increase the energy density and power density of the electrode active materials. As a positive electrode active materials for LIBs, $\text{LiNi}_{0.5}\text{Mn}_{1.5}\text{O}_4$ has been widely investigated for its high operation voltage (high energy density) and facile three dimensional lithium-ion diffusion (high power)^{1–5}.

Based on a mechanism analogous to the Kirkendall effect, a hollow structured $\text{LiNi}_{0.5}\text{Mn}_{1.5}\text{O}_4$ has been synthesized by a facile impregnation approach⁶. The hollow structured $\text{LiNi}_{0.5}\text{Mn}_{1.5}\text{O}_4$ exhibits superior electrochemical performance. On the other hand, hollow manganese oxides microstructures can be synthesized by a simple method from MnCO_3 ^{7,8}. Here, we present a strategy to controllably synthesize $\text{LiNi}_{0.5}\text{Mn}_{1.5}\text{O}_4$ with various microstructures by using manganese compounds with different microstructures. The effects of microstructures on performance of $\text{LiNi}_{0.5}\text{Mn}_{1.5}\text{O}_4$ were investigated systematically.

$\text{LiNi}_{0.5}\text{Mn}_{1.5}\text{O}_4$ containing only Mn^{4+} has a poor electronic conductivity because active $\text{Ni}^{2+/3+/4+}$ redox centers are isolated among the inactive Mn^{4+} nearest neighbors^{9,10}. $\text{LiNi}_{0.5}\text{Mn}_{1.5}\text{O}_4$ spinels with

¹School of Chemical Engineering and Technology, Harbin Institute of Technology, No. 92 West-Da Zhi Street, Harbin, 150001 China. ²Chilwee Power Co. Ltd., No. 12 Zhizhou Road, Xinxing Industrial Park, Zhicheng, Changxing, Zhejiang Province 313100, China. Correspondence and requests for materials should be addressed to Z.W. (email: wangzhib@hit.edu.cn)

presence of Mn^{3+} exhibit better rate performance due to a higher electronic and lithium-ion conductivity^{11,12}. However, Mn^{3+} ions are unstable and tend to undergo a disproportionation reaction: $2\text{Mn}^{3+} = \text{Mn}^{2+} + \text{Mn}^{4+}$. The produced Mn^{2+} ions then dissolve into the electrolyte, leading to a capacity fading during charging-discharging cycling^{13,14}. In the $\text{LiNi}_{0.5}\text{Mn}_{1.5}\text{O}_4$ products, $\text{Li}_x\text{Ni}_{1-x}\text{O}$ usually appears as impurity phase, lowering the capacity and blocking Li^+ mobility in the material. In other words, Mn^{3+} and impurity in the spinel have great effects on the electrochemical properties. Therefore, it is crucial to find out the reasons of forming Mn^{3+} and impurity in the spinel product and control their content^{15–17}. Loss of oxygen occurring at high-temperature calcination will obviously lead to the appearance of impurity phase and Mn^{3+} in the spinel. The oxygen loss is reversible and can be recovered by annealing, which can also reduce impurity and Mn^{3+} content^{18,19}. Besides, Mn^{3+} and impurity content in the spinel is affected by a cation doping^{20,21}. Here, for the first time, we have revealed that an inhomogeneous atoms migration may also introduce Mn^{3+} and impurity phase in the spinel.

Experimental

Preparation of precursors with different microstructures. Firstly, solid MnCO_3 spheres were synthesized by a precipitation method described as below. 200 mL ethanol was added to a MnSO_4 solution (0.04 mol L^{-1} , 1 L) to form a mixture. A NH_4HCO_3 solution (0.4 mol L^{-1} , 1 L) was added to the mixture solution dropwisely under stirring. The mixture was kept stirring for 5 h. Then the produced precipitate was collected and dried at 60°C to obtain solid spherical MnCO_3 .

The obtained MnCO_3 was treated by different methods to change the microstructure. MnO_2 with a hollow microstructure was synthesized by calcinating the solid MnCO_3 spheres at 350°C for 4 h with a subsequent acid-washing. 0.1 mol L^{-1} HCl solution was employed in the acid-washing process. Mn_2O_3 with a hierarchical microstructure was synthesized by calcinating the solid MnCO_3 spheres at 800°C for 4 h.

Preparation of $\text{LiNi}_{0.5}\text{Mn}_{1.5}\text{O}_4$ with different microstructures. $\text{LiNi}_{0.5}\text{Mn}_{1.5}\text{O}_4$ spinels with various microstructures were prepared by using the above-mentioned solid MnCO_3 spheres, hollow MnO_2 and hierarchical Mn_2O_3 as precursors respectively. Stoichiometric amounts of $\text{LiOH}\cdot\text{H}_2\text{O}$, $\text{Ni}(\text{NO}_3)_2\cdot 6\text{H}_2\text{O}$ and the corresponding precursor taken in the ratio $\text{Li}:\text{Ni}:\text{Mn} = 1.05:0.5:1.5$ were dispersed in ethanol. The dispersion was stirred to mix the reactants and the ethanol was evaporated slowly at room temperature under stirring. The mixture obtained after evaporation was calcined at 850°C for 10 hours and then cooled at a rate of $0.5^\circ\text{C min}^{-1}$ in the air to obtain the product. The product was solid $\text{LiNi}_{0.5}\text{Mn}_{1.5}\text{O}_4$ spheres (denoted as SO-LNMO), hollow $\text{LiNi}_{0.5}\text{Mn}_{1.5}\text{O}_4$ (denoted as HO-LNMO) and hierarchical $\text{LiNi}_{0.5}\text{Mn}_{1.5}\text{O}_4$ (denoted as HI-LNMO), corresponding to the precursor of solid MnCO_3 spheres, hollow MnO_2 and hierarchical Mn_2O_3 , respectively.

Characterization. The obtained materials were characterized by scanning electron microscopy (SEM), X-ray photoelectron spectroscopy (XPS) and powder X-ray diffraction (XRD). XRD characterization was carried out with a D/max-RB diffractometer using a $\text{Cu K}\alpha$ source and recorded with a step of 0.05° . XPS characterization was carried out with Thermofisher Scientific, K-Alpha. Brunauer–Emmett–Teller (BET) specific surface area was tested by using Beishide 3H-2000Ps1. And the Raman spectra were obtained with a Renishaw in Via Raman microscope. The synthesized samples were analyzed by inductively coupled plasma (ICP, PerkinElmer, Optima 5300DV) tests.

Electrochemical tests of the homemade samples were carried out by using coin-type cells (2025). The cathode materials of the cells were made from a slurry containing 80 wt.% active material, 10 wt.% conductive acetylene black as conductive agent and 10 wt.% polyvinylidene fluoride (PVDF) as binder dissolved in *n*-methyl pyrrolidinone. The slurry was evenly coated onto an aluminum foil by using a blade and then dried in a vacuum oven at 120°C for overnight. Then the foil was punched into a circular electrode (1.4 cm in diameter). The loading weight of the active materials on the electrode was about 2 mg cm^{-2} . Cells with lithium metal as the counter electrode were assembled in an argon-filled glove box. The electrolyte was 1 mol L^{-1} LiPF_6 in a mixture of ethylene carbonate and dimethyl carbonate with a ratio of 1:1 by weight. Charge-discharge tests were carried out on a NEWWARE battery tester. When the current densities were higher than 0.5 C, the cells were charged galvanostatically to 4.95 V and the cell voltage was kept at 4.95 V until the current decreased to 0.1 C. Then the cells were discharged to 3.5 V at different rates. Cyclic voltammetry (CV: 3.5–5.1 V, 0.1 mV s^{-1}) and electrochemical impedance spectroscopy (EIS) was carried out on a CHI650D electrochemical workstation. EIS measurements were conducted with an AC amplitude of 5 mV at 4.73 V in the frequency range from 10^5 Hz to 0.01 Hz .

Results and Discussion

The procedure of microstructure-controllably preparing $\text{LiNi}_{0.5}\text{Mn}_{1.5}\text{O}_4$ is illustrated in Figure S1 in Supporting Information. As is shown, the microstructures of $\text{LiNi}_{0.5}\text{Mn}_{1.5}\text{O}_4$ can be controlled by using manganese compound with different microstructures as precursor.

Precursors with different microstructures obtained at different conditions. The produced precursors were characterized by XRD and SEM, as shown in Figure S2 and Fig. 1.

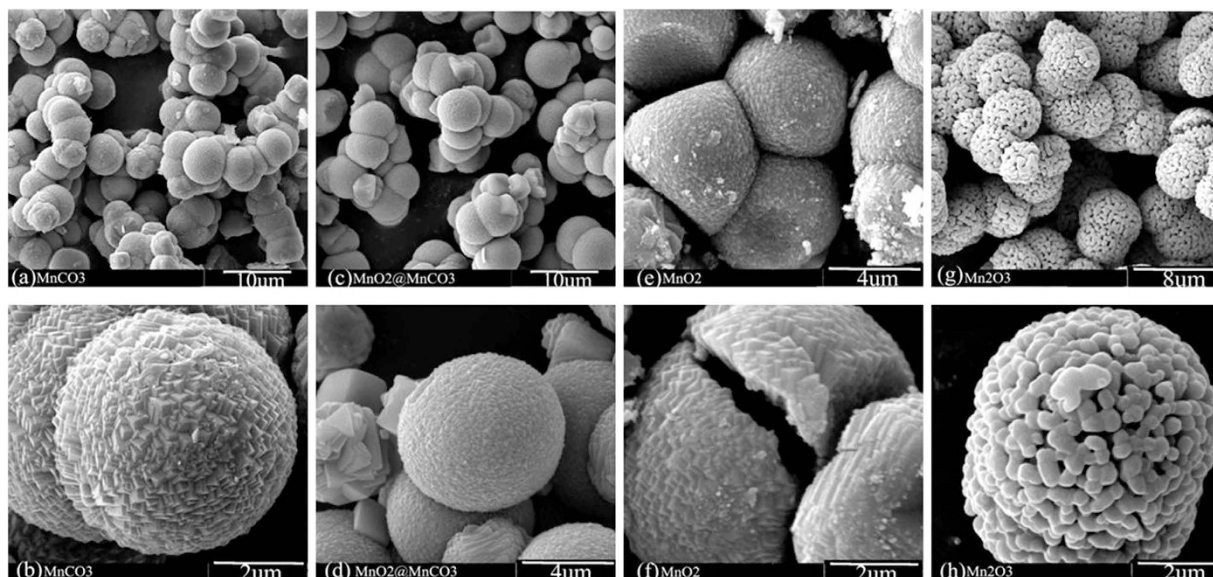


Figure 1. SEM micrographs of materials obtained during the procedure of synthesizing precursors: (a,b) MnCO_3 precipitate before calcination, (c,d) $\text{MnO}_2/\text{MnCO}_3$ composite obtained after calcinating the precipitate at 350°C , (e,f) MnO_2 obtained after acid-washing the $\text{MnO}_2/\text{MnCO}_3$ mixture and (g,h) Mn_2O_3 obtained after calcinating the MnCO_3 precipitate at 800°C .

Solid spheres, the precipitate before calcination, shown in Fig. 1(a,b) are synthesized by a precipitation reaction between MnSO_4 and NH_4HCO_3 . The XRD pattern (Figure S2(a)) of the obtained precipitate can be assigned to MnCO_3 . The MnCO_3 precipitate appears to be solid microspheres with a diameter of $\sim 5\ \mu\text{m}$.

After the MnCO_3 spheres was calcined at 350°C for 4 h, the XRD pattern in Figure S2(b) indicates that the MnCO_3 precipitate turns into a mixture of MnCO_3 and MnO_2 . The MnCO_3 precipitate was partially decomposed to MnO_2 whereas the inner core remains to be MnCO_3 ⁷. MnCO_3 can be easily dissolved in a diluted acid, whereas MnO_2 cannot. Therefore, after acid-washing the partially decomposed samples, the MnCO_3 residual almost disappeared as indicated by a weakened MnCO_3 peaks in the XRD pattern in Figure S2(c) and the MnO_2 peaks remains without obvious change. In addition, a weight loss of the sample after acid-washing also supports the dissolution of the undecomposed MnCO_3 . The morphology of the sample after acid-washing is shown in Fig. 1(e,f). The particles have spherical shape with a hollow microstructure seen from the cracked particle.

After the precipitate MnCO_3 spheres was calcined at 800°C for 4 h, it turns into Mn_2O_3 as indicated by the XRD pattern shown in Figure S2(d). Different from the calcinations at 350°C , the microstructure of the produced Mn_2O_3 particles changed into a submicro/micro hierarchical structure after calcination at 800°C , as shown in Fig. 1(g,h). The primary particle size of the Mn_2O_3 is about 400 nm and the secondary particles are microspheres with diameters of $\sim 5\ \mu\text{m}$. It is worth noting that the primary particles are interconnected, rather than closely piled up. It is attributed to that the hierarchical Mn_2O_3 microstructure is formed by a volume shrinkage of the MnCO_3 microsphere occurred at calcinations.

$\text{LiNi}_{0.5}\text{Mn}_{1.5}\text{O}_4$ with different microstructures produced from different precursors. The SO-LNMO, HO-LNMO and HI-LNMO are synthesized by using the above-mentioned solid MnCO_3 spheres, hollow MnO_2 and hierarchical Mn_2O_3 as precursors, respectively. Figure 2 shows SEM images of these produced $\text{LiNi}_{0.5}\text{Mn}_{1.5}\text{O}_4$ materials. All the three samples remain the spherical shape of the precursors.

As shown in Fig. 2(a,b), the SO-LNMO particle prepared with the solid-sphere-structured precursor are solid seen from the section of particles. As shown in Fig. 2(c,d), the HO-LNMO particle prepared with the hollow-sphere-structured precursor has a similar hollow microstructure with a dense shell ($\sim 1\ \mu\text{m}$ in thickness). As shown in Fig. 2(e,f), the HI-LNMO particle prepared with the hierarchical-structured precursor has a similar submicro/micro hierarchical structure with the primary particles connected. The primary particle size is about 500 nm and the secondary particle is in a shape of microsphere with a diameter of $\sim 5\ \mu\text{m}$.

By a comparison of the microstructure between the $\text{LiNi}_{0.5}\text{Mn}_{1.5}\text{O}_4$ products and their precursors, it can be seen that the particle microstructure of the produced $\text{LiNi}_{0.5}\text{Mn}_{1.5}\text{O}_4$ remains almost the same as their precursors' microstructures. So it is a feasible way to control the microstructures of $\text{LiNi}_{0.5}\text{Mn}_{1.5}\text{O}_4$ by controlling their precursors' microstructures.

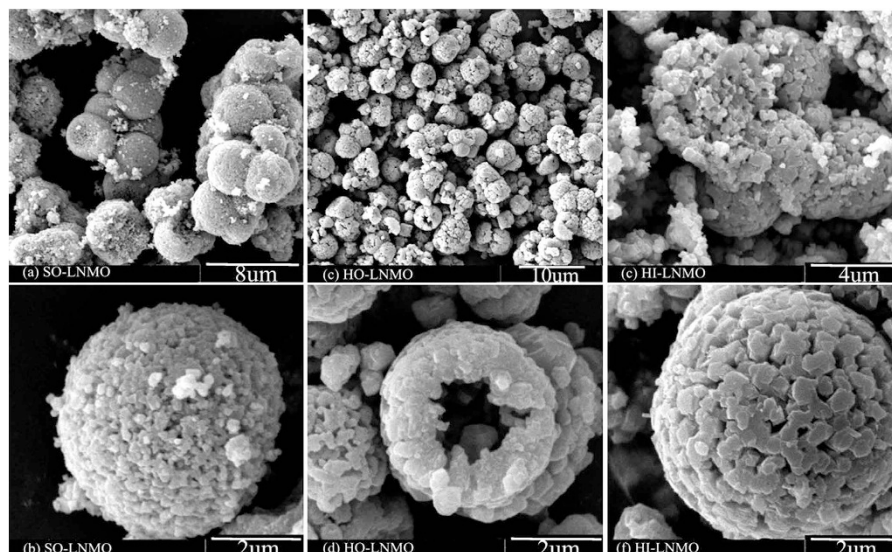


Figure 2. SEM micrographs of (a,b) SO-LNMO prepared from a solid-structured precursor, (c,d) HO-LNMO prepared from a hollow-structured precursor and (e,f) HI-LNMO prepared from a hierarchical-structured precursor.

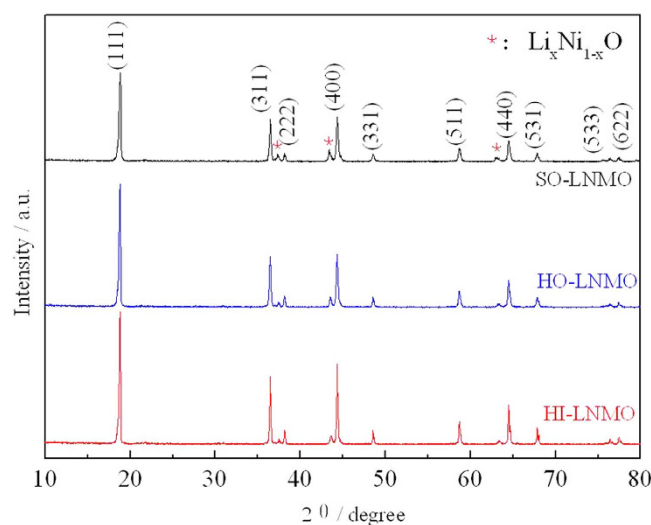


Figure 3. XRD patterns of $\text{LiNi}_{0.5}\text{Mn}_{1.5}\text{O}_4$ with different microstructures.

Figure 3 shows the XRD patterns of the $\text{LiNi}_{0.5}\text{Mn}_{1.5}\text{O}_4$ products with different microstructures. All the three patterns can be assigned to a cubic spinel $\text{LiNi}_{0.5}\text{Mn}_{1.5}\text{O}_4$. Besides, some weak peaks at $2\theta = 37.5$, 43.6 and 63.4° can be attributed to a $\text{Li}_x\text{Ni}_{1-x}\text{O}$ impurity phase²². The content of impurity phase is estimated by calculating the ratio of peak intensity at $2\theta = 43.6^\circ$ of impurity phase to that at $2\theta = 44.3^\circ$ of spinel phase. The intensity ratios in the SO-LNMO, HO-LNMO and HI-LNMO products are 28.1:100, 17.9:100 and 10.4:100, respectively. Impurity content in the three samples decreases in the following order: SO-LNMO > HO-LNMO > HI-LNMO.

With disordered Ni and Mn on the octahedral sites, the cubic spinels have the space group $\text{Fd}\bar{3}\text{m}$, but the ordering of Ni and Mn in $\text{LiNi}_{0.5}\text{Mn}_{1.5}\text{O}_4$ gives the space group $\text{P}4_3\bar{3}2$. Raman spectroscopy is a useful tool to determine the cation ordering. Figure S3 shows Raman spectra of the samples. The peaks around 635 cm^{-1} are assigned to the symmetric Mn-O stretching vibration of MnO_6 group and the peaks around 400 and 490 cm^{-1} can be assigned to the Ni-O stretching mode. The Raman spectra of the three samples are indexed to $\text{Fd}\bar{3}\text{m}$ space group, due to the absence of a splitting of peaks in the $588\text{--}623\text{ cm}^{-1}$ region, which are characteristic of the ordered structure ($\text{P}4_3\bar{3}2$) of the spinel^{23,24}.

Cyclic voltammetry (CV) curves of the homemade $\text{LiNi}_{0.5}\text{Mn}_{1.5}\text{O}_4$ with different microstructures before and after 200 cycles at a rate of 2 C are compared (shown in Fig. 4). For all the three samples, the main peaks around 4.7 V are attributed to a $\text{Ni}^{2+}/\text{Ni}^{4+}$ redox couple and the weak peaks at 4.0 V

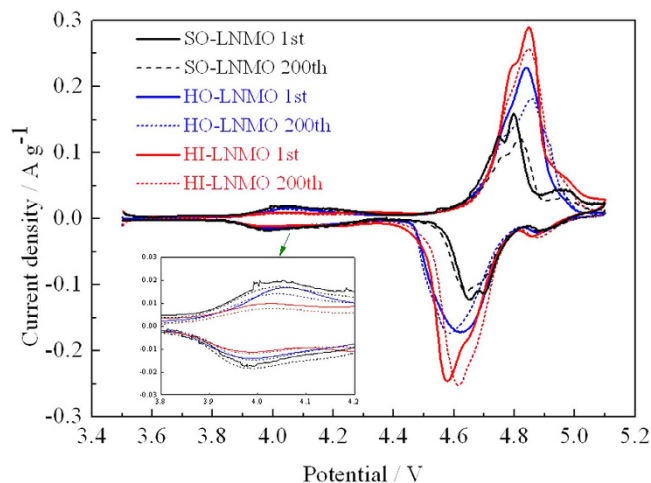


Figure 4. Cyclic voltammetry curves of $\text{LiNi}_{0.5}\text{Mn}_{1.5}\text{O}_4$ with different microstructures before and after 200 cycles at a rate of 2 C.

are attributed to a $\text{Mn}^{3+}/\text{Mn}^{4+}$ redox couple. Among the three samples, the peak area around 4.7 V of HI-LNMO is the largest, indicating that HI-LNMO has the highest electrolyte-accessible surface area due to its particle microstructure. Obviously, a large specific electrochemically active surface area is beneficial to high rate capability. This will be discussed later. On the other hand, the peaks area at 4.0 V is related to the Mn^{3+} content in spinel²⁵. Through comparing the peak area at 4.0 V, the Mn^{3+} content in $\text{LiNi}_{0.5}\text{Mn}_{1.5}\text{O}_4$ is in an order as below: SO-LNMO > HO-LNMO > HI-LNMO.

In order to compare the rate capability among the three $\text{LiNi}_{0.5}\text{Mn}_{1.5}\text{O}_4$ samples, the cells were cycled at various rates ranging from 0.2 to 15 C. The cells were charged at 1 C rate when the discharging current densities were higher than 0.5 C. Figure 5 displays the charging and discharging curves of the three $\text{LiNi}_{0.5}\text{Mn}_{1.5}\text{O}_4$ samples with different microstructures. The curves at low discharging rates show a dominant plateau at around 4.7 V, which is attributed to a $\text{Ni}^{2+}/\text{Ni}^{4+}$ redox couple. A minor plateau in 4 V region is also observed associated with the $\text{Mn}^{3+}/\text{Mn}^{4+}$ redox couple. The length of 4 V plateau in discharging curves can be used to evaluate the relative Mn^{3+} content in the spinel^{26,27}. The proportion of discharge capacity in 3.8~4.2 V region at 0.2 C for SO-LNMO, HO-LNMO and HI-LNMO are 17.9%, 10.0% and 7.0%, respectively. This means that Mn^{3+} content in the three samples is in the following order: SO-LNMO > HO-LNMO > HI-LNMO, which is consistent with the estimated results from CV curves.

From above results, it can be seen that the Mn^{3+} and impurity contents in the three samples both are in an order as below: SO-LNMO > HO-LNMO > HI-LNMO. Generally, it is believed that the appearance of Mn^{3+} and impurity phase is caused by a loss of oxygen at high-temperature calcination. So the content of the impurity phase and Mn^{3+} in spinel is affected by calcining and annealing conditions. In this work, however, the calcining and annealing conditions were kept the same for all the three spinel samples. So the difference in the Mn^{3+} and impurity contents among these three samples are rather related to some difference of their precursor particles' microstructures.

During the synthesis process, precursor, $\text{Ni}(\text{NO}_3)_2$ and LiOH were dispersed into ethanol to mix these reactants, in which all the $\text{Ni}(\text{NO}_3)_2$ and a part of LiOH dissolved in ethanol. After the evaporation of ethanol, dissolved $\text{Ni}(\text{NO}_3)_2$ will deposit on the precursors' surface. SEM images of the mixture after mixing process are shown in Figure S4. The distribution of the Ni element depends on the precursor particles' microstructure. The schematic distribution of Ni and Mn elements in the mixture after the evaporation in different methods is shown in Figure S5.

In the case of using solid-sphere-structured precursor, most of the $\text{Ni}(\text{NO}_3)_2$ deposits on the outer surface of solid MnCO_3 microspheres as illustrated in Figure S4(a) and Figure S5. During the subsequent high-temperature calcination, Ni and Mn atoms have to migrate over a distance as long as several micrometers to form a homogeneous $\text{LiNi}_{0.5}\text{Mn}_{1.5}\text{O}_4$ phase. This long distance leads to an inhomogeneous elements' distribution even after calcinations. There will be relatively more Ni element in the surface, resulting in high impurity content and more Mn element in interior, resulting in high Mn^{3+} content of the produced SO-LNMO.

In the case of hollow-structured precursor, $\text{Ni}(\text{NO}_3)_2$ deposits on both the outer and the inner surfaces of the hollow-sphere' shell as illustrated in Figure S4(b) and Figure S5. The distance for the migration of Ni and Mn atoms is reduced to at least half of that in the above-mentioned solid-sphere-structured precursor. As a result, the content of Mn^{3+} and impurity phase is expected to be lower than that in the SO-LNMO, which is supported by the actual results of the order in Mn^{3+} and impurity content.

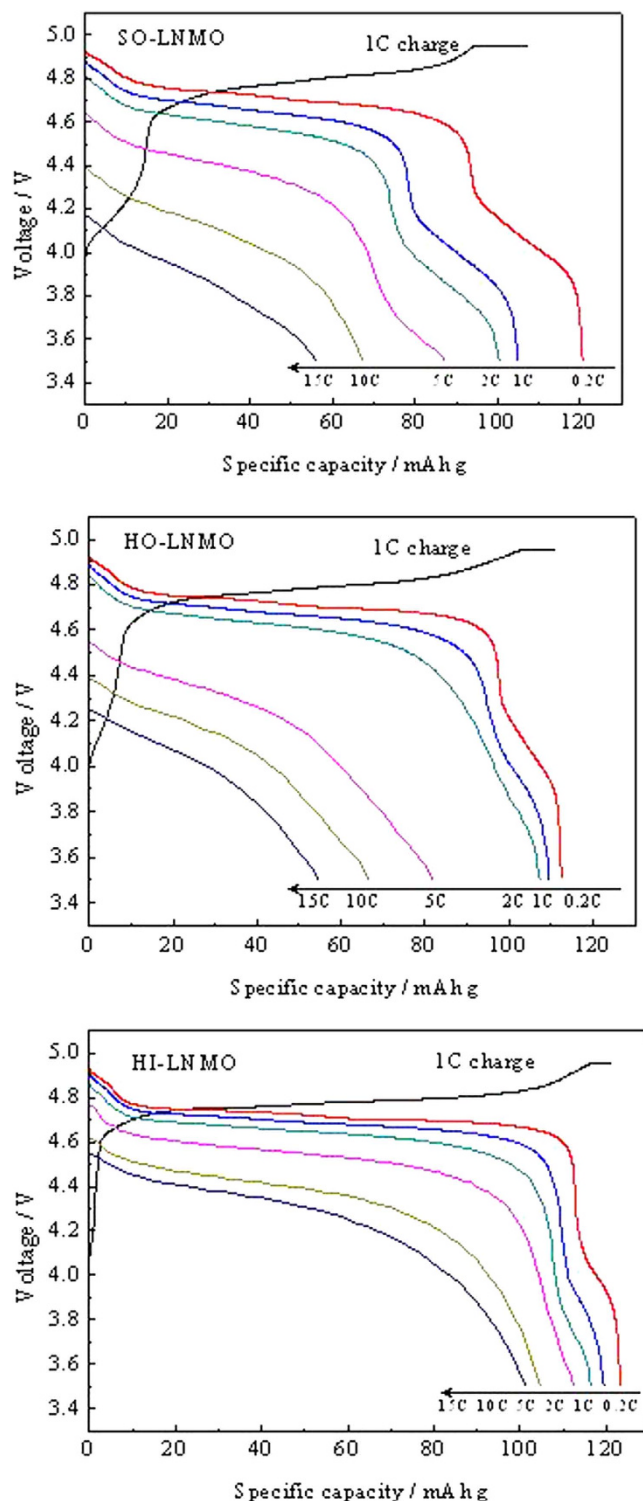


Figure 5. Charge and discharge capacity curves of $\text{LiNi}_{0.5}\text{Mn}_{1.5}\text{O}_4$ with different microstructures.

In the case of hierarchical-structured precursor, $\text{Ni}(\text{NO}_3)_2$ could deposit in submicro-sized space between the primary particles as illustrated in Figure S4(b) and Figure S5. The distance of the migration for Ni and Mn atoms could be reduced to the primary-particle-size level, much shorter than the above-mentioned two cases, leading to an inhomogeneous elements' distribution. Therefore, HI-LNMO has the lowest Mn^{3+} and impurity contents.

To further verify the above discussion about the reason of forming Mn^{3+} and impurity in the spinel, $\text{LiNi}_{0.5}\text{Mn}_{1.5}\text{O}_4$ products after calcinations were characterized by XPS²⁸. The Ni $2p_{3/2}$ and Mn $2p_{3/2}$ spectra are shown in Fig. 6. The ratio of peak area of Ni $2p_{3/2}$ to that of Mn $2p_{3/2}$ in the SO-LNMO, HO-LNMO

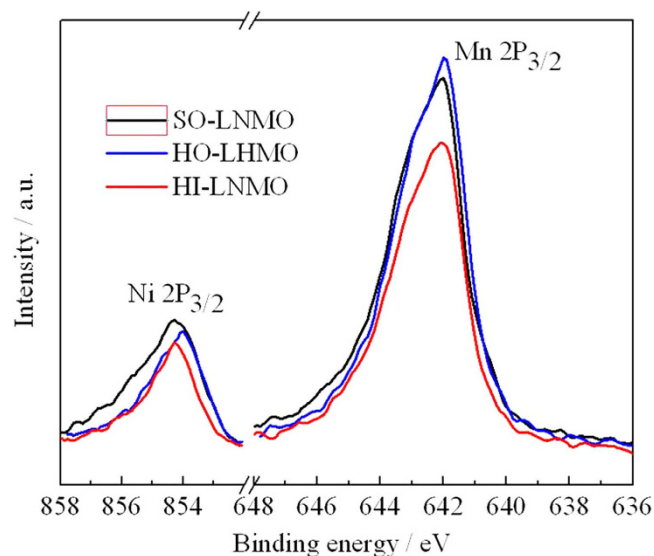


Figure 6. Ni $2p_{3/2}$ and Mn $2p_{3/2}$ XPS spectra of $\text{LiNi}_{0.5}\text{Mn}_{1.5}\text{O}_4$ with different microstructures.

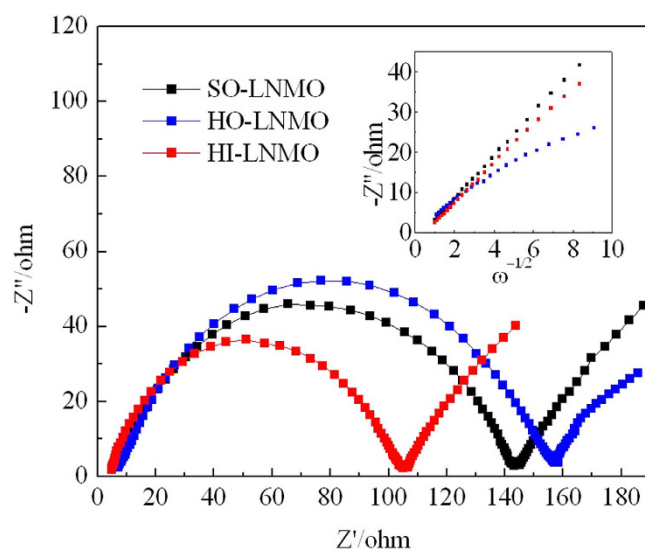


Figure 7. Electrochemical impedance spectroscopy of $\text{LiNi}_{0.5}\text{Mn}_{1.5}\text{O}_4$ with different microstructures.

and HI-LNMO products are 30.9:100, 25.7:100 and 24.5:100, respectively. This result indicates that the Ni content in the surface of SO-LNMO is the highest, which is consistent with the above discussion. The Mn and Ni contents of samples were analyzed by ICP and the results are shown in Table S1. The molar ratios of Mn/Ni in the SO-LNMO, HO-LNMO and HI-LNMO are 3.10, 3.21 and 3.10, respectively. The molar ratios of Mn/Ni in the SO-LNMO and HI-LNMO are same. The molar ratios of Mn/Ni in the samples are inconsistent with the molar ratios of Mn/Ni in the surface. So the difference in distribution of Ni and Mn on the surface come from inhomogeneous migration of atoms, rather than the cation composition in the initial mixtures of reagents.

Besides, the $\text{Mn}^{3+}/\text{Mn}^{4+}$ ratio in the surface was estimated by Mn $2p_{3/2}$ XPS curve fitting²⁹, shown in Figure S6. Mn^{4+} and Mn^{3+} each give rise to the Mn $2p_{3/2}$ binding energies at 642.9 and 641.9 eV. The ratio of peak area of Mn^{4+} to that of Mn^{3+} in the SO-LNMO, HO-LNMO and HI-LNMO are 39.8:100, 49.4:100 and 49.2:100, respectively. This result indicates that the Mn^{3+} content in the surface of SO-LNMO is the lowest. However, the CV curves and discharging curves have shown that the Mn^{3+} content in SO-LNMO is the highest. It means that the excess Mn^{3+} exists in interior of particles, which is consistent with the above discussion.

The electrochemical impedance spectroscopy measurements were performed on the cells. And the Nyquist plots are shown in Fig. 7. As shown, each plot consists of a depressed semicircle in the high frequency region and a sloping line at low frequency range. The depressed semicircle reflects the interface

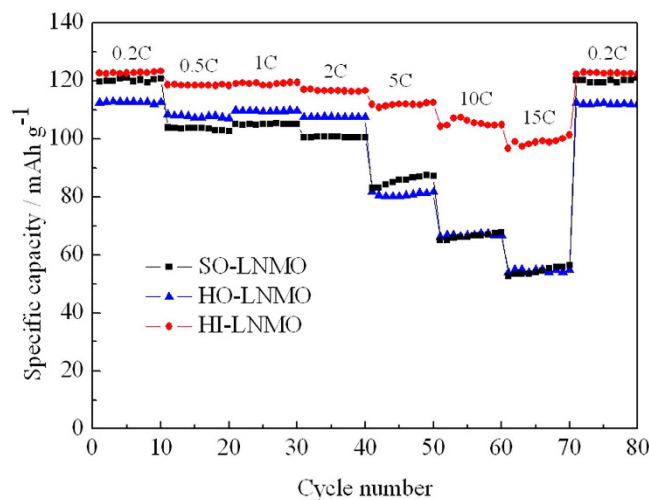


Figure 8. Rate capability of $\text{LiNi}_{0.5}\text{Mn}_{1.5}\text{O}_4$ with different microstructures.

impedance, including interfacial layer and charge transfer reaction and the sloping line reflects the diffusion of Li-ion in the solid electrode, respectively^{30,31}. It can be seen that the interface impedance of HI-LNMO is the smallest.

The Warburg coefficient (B) can be obtained from the slope of $-Z'' = B\omega^{-1/2}$, showed in inset of Fig. 7. The Warburg coefficient (B) of SO-LNMO, HO-LNMO and HI-LNMO are 5.3, 4.8 and 2.8, respectively. Then the Li-ion diffusion coefficient can be estimated from Eq.(1)³², where V_m is molar volume of the spinel material, S is the electrolyte-accessible surface area of the electrode and $(dE)/(dx)$ is the slope of the open-circuit potential vs. mobile ion concentration x . Because the three samples are all $\text{LiNi}_{0.5}\text{Mn}_{1.5}\text{O}_4$, V_m , F and $(dE)/(dx)$ in Eq(1) are similar. The Li-ion diffusion coefficient depends on the value of S and B . With the similar value of B , the electrolyte-accessible surface area of HI-LNMO is much larger than that of SO-LNMO. So the Li-ion diffusion coefficient of HI-LNMO is lower, due to its lower Mn^{3+} content.

$$D_{\text{Li}} = 0.5 \left[\frac{V_m}{FSB} \left(-\frac{dE}{dx} \right) \right]^2 \quad (1)$$

The rate capability of the $\text{LiNi}_{0.5}\text{Mn}_{1.5}\text{O}_4$ products with different microstructures are compared and shown in Fig. 8. As can be clearly seen, HI-LNMO exhibits the best high-rate performance. HI-LNMO is still able to deliver a high specific capacity over 100 mAh g^{-1} at 15 C, equivalent to as high as 82.1% of discharge capacity at 0.2 C. However, SO-LNMO and HO-LNMO show poor high rate performance, the discharge capacity at 15 C drops to as low as 45.4% and 50.1% of that at 0.2 C, respectively. Mn^{3+} in spinel can enhance the conductivity, which is beneficial to high rate performance^{11,12}. However, as discussed above, HI-LNMO with the lowest content of Mn^{3+} unexpectedly exhibits the best high-rate performance. Therefore, this good high-rate performance of HI-LNMO could be attributed to its hierarchical microstructure, illustrated in Figure S7, in which the submicrometer-sized primary particles obviously increase the active specific surface area for electrochemical reactions and shorten the diffusion distance for Li^+ ions. On the other hand, it is difficult for all the primary particles to electronically contact with conducting agents uniformly. Large current will flow through the places contact with conducting agent. The connected microstructure makes every primary particle share the current and be charged/discharged efficiently. Generally, a high overpotential occurs on the particle due to the relatively high resistance which comes from a high interface resistance between the primary particles. However, in the case of hierarchical microstructure, the interface resistance between the primary particles is lower because they interconnect to each other with less interface rather than contact with interface. In other words, the good high-rate performance of HI-LNMO is partly attributed to its higher conductivity between the primary particles.

The excellent high-rate performance of HI-LNMO is further demonstrated, as shown in Figure S8, by the lowest charging plateau voltage and the highest discharging plateau voltage at the same charging/discharging rate of 5 C in cycling tests, indicating the smallest polarization.

Although rate performance can be significantly improved by preparing nanosized materials^{33,34}, the application of nanosized materials is challenged by the following two facts: (1) they cannot be coated on the current collector as densely as micrometer-sized materials³⁵, which reduces the energy density and (2) the very large specific surface area of nanosized materials cause more side reactions such as decomposition of the electrolyte and dissolution of Mn, leading to a lower durability and cycling stability³⁶. Here, HI-LNMO with excellent rate capability has a BET specific surface area of as low as $2.1 \text{ m}^2 \text{ g}^{-1}$.

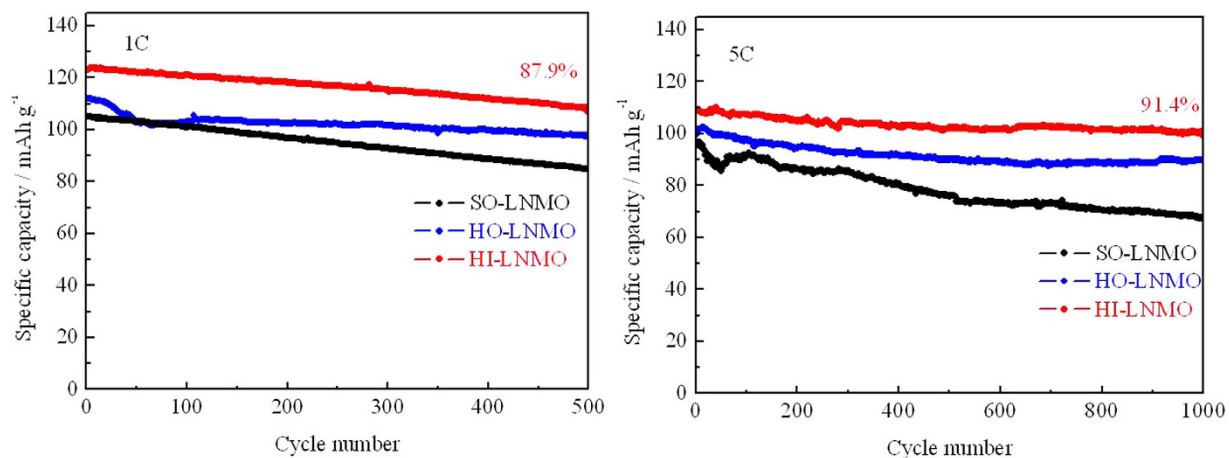


Figure 9. Cycling performance of $\text{LiNi}_{0.5}\text{Mn}_{1.5}\text{O}_4$ with different microstructures rates of 1 C and 5 C.

Compared with nano-sized materials ($15.5 \text{ m}^2 \text{ g}^{-1}$)³³, this relatively small specific surface area is expected to promote the cycling performance and durability.

The cycling performances at various charging/discharging rates (1 C and 5 C) of the homemade $\text{LiNi}_{0.5}\text{Mn}_{1.5}\text{O}_4$ with different microstructures are compared, as shown in Fig. 9. After 500 cycles at 1C and 1000 cycles at 5 C, HI-LNMO shows the highest discharge capacity and the best capacity retention among the three samples. The excellent cycling performance of HI-LNMO is attributed to the following two factors: (1) a lower content of Mn^{3+} which decreases the speed of Mn dissolution and Jahn-Teller distortion and (2) the existence of space among the primary particles in the hierarchical microstructure which can buffer the volume change occurring in Li^+ insertion/extraction process.

Interestingly, for HI-LNMO, the capacity retention after 1000 cycles at 5C is 91.4%, higher than 87.9% after 500 cycles at 1C. That is, the same sample HI-LNMO cycled at a larger current density unexpectedly shows a higher capacity retention after more cycles. This indicates that an irreversible structure change during the repeated Li^+ insertion/extraction, which usually occurs more seriously during cycling at a higher rate, is not the dominant factor for capacity fading. It should be pointed out that it takes only 582 hours for 1000 cycles at 5C, approximately as half as 1067 hours for 500 cycles at 1C. It means that regardless of a lower current density and less cycle numbers, a longer duration of experimental process leads to a more serious capacity fading. In other words, the side reactions between the electrode and the electrolyte are the dominant factor for capacity fading. This supports that there is a trade-off between the lifetime and the high-rate performance in terms of the optimized specific surface area.

Conclusions

$\text{LiNi}_{0.5}\text{Mn}_{1.5}\text{O}_4$ micro-particles with solid, hollow and hierarchical microstructures were synthesized separately and compared. The following conclusions could be made. (1) It is a feasible way to control the particle microstructure of $\text{LiNi}_{0.5}\text{Mn}_{1.5}\text{O}_4$ spinel by using manganese compounds as precursors and controlling the microstructures of the precursors. (2) An inhomogeneous migration of Ni and Mn atoms could introduce Mn^{3+} and impurity phase in the spinel product. (3) A hierarchical microstructure with the primary particles interconnected has small interface resistance. The space in the secondary particles can accommodate electrolyte and buffer volume change during cycling. Together with its appropriate specific surface area, HI-LNMO has both optimized rate capability and cycling stability. (4) Side reactions between the electrode and the electrolyte, rather than repeated Li^+ insertion/extraction, is the dominant factor for capacity fading during cycling.

References

- Kim, J. H. *et al.* Comparative study of $\text{LiNi}_{0.5}\text{Mn}_{1.5}\text{O}_{4.8}$ and $\text{LiNi}_{0.5}\text{Mn}_{1.5}\text{O}_4$ cathodes having two crystallographic structures: Fd3m and P432. *Chem. Mater* **16**, 906–914 (2004).
- Hassoun, J., Lee, K. S., Sun, Y. K. & Scrosati, B. An advanced lithium ion battery based on high performance electrode materials. *J. Am. Chem. Soc.* **133**, 3139–3143 (2011).
- Jung, H. G., Jang, M. W., Hassoun, J., Sun, Y. K. & Scrosati, B. A high-rate long-life $\text{Li}_4\text{Ti}_5\text{O}_{12}/\text{Li}[\text{Ni}_{0.45}\text{Co}_{0.1}\text{Mn}_{1.45}]\text{O}_4$ lithium-ion battery. *Nat. commun.* **2**, 516–520 (2011).
- Goodenough, J. B. & Park, K. S. The Li-ion rechargeable battery: a perspective. *J. Am. Chem. Soc.* **135**, 1167–1176 (2013).
- Goodenough, J. B. Electrochemical energy storage in a sustainable modern society. *Energy Environ. Sci.* **7**, 14–18 (2014).
- Zhou, L., Zhao, D. & Lou, X. W. $\text{LiNi}_{0.5}\text{Mn}_{1.5}\text{O}_4$ Hollow structures as high-Performance cathodes for Lithium-Ion batteries. *Angew. Chem.* **124**, 243–245 (2012).
- Wang, L. *et al.* A general single source route for the preparation of hollow nanoporous metal oxide structures. *Angew. Chem.* **121**, 7182–7185 (2009).
- Fei, J. B. *et al.* Controlled preparation of MnO_2 hierarchical hollow nanostructures and their application in water treatment. *Adv. Mater* **20**, 452–456 (2008).

9. Lee, E. S., Nam, K. W., Hu, E. & Manthiram, A. Influence of cation ordering and lattice distortion on the charge–discharge behavior of $\text{LiMn}_{1.5}\text{Ni}_{0.5}\text{O}_4$ spinel between 5.0 and 2.0 V. *Chem. Mater* **24**, 3610–3620 (2012).
10. Shin, D. W., Bridges, C. A., Huq, A., Paranthaman, M. P. & Manthiram, A. Role of cation ordering and surface segregation in high-voltage spinel $\text{LiMn}_{1.5}\text{Ni}_{0.5-x}\text{M}_x\text{O}_4$ ($M = \text{Cr, Fe and Ga}$) cathodes for Lithium-ion batteries. *Chem. Mater* **24**, 3720–3731 (2012).
11. Kunduraci, M. & Amatucci, G. G. Synthesis and characterization of nanostructured 4.7 V $\text{Li}_x\text{Mn}_{1.5}\text{Ni}_{0.5}\text{O}_4$ spinels for high-power Lithium-ion batteries. *J. Electrochem. Soc.* **153**, A1345–A1352 (2006).
12. Kunduraci, M. & Amatucci, G. G. The effect of particle size and morphology on the rate capability of 4.7 V $\text{LiMn}_{1.5+x}\text{Ni}_{0.5-x}\text{O}_4$ spinel lithium-ion battery cathodes. *Electrochim. Acta* **53**, 4193–4199 (2008).
13. Park, O. K. *et al.* Who will drive electric vehicles, olivine or spinel? *Energy Environ. Sci.* **4**, 1621–1633 (2011).
14. Pieczonka, N. P. *et al.* Understanding transition-Metal dissolution behavior in $\text{LiNi}_{0.5}\text{Mn}_{1.5}\text{O}_4$ high-voltage spinel for lithium ion batteries. *J. Phys. Chem. C* **117**, 15947–15957 (2013).
15. Xiao, J. *et al.* High-performance $\text{LiNi}_{0.5}\text{Mn}_{1.5}\text{O}_4$ spinel controlled by Mn^{3+} concentration and site disorder. *Adv. Mater* **24**, 2109–2116 (2012).
16. Manthiram, A., Chemelewski, K. & Lee, E. S. A perspective on the high-voltage $\text{LiMn}_{1.5}\text{Ni}_{0.5}\text{O}_4$ spinel cathode for lithium-ion batteries. *Energy Environ. Sci.* **7**, 1339–1350 (2014).
17. Xue, Y., Wang, Z., Yu, F., Zhang, Y. & Yin, G. Ethanol-assisted hydrothermal synthesis of $\text{LiNi}_{0.5}\text{Mn}_{1.5}\text{O}_4$ with excellent long-term cyclability at high rate for lithium-ion batteries. *J. Mater. Chem. A* **2**, 4185–4191 (2014).
18. Song, J. *et al.* Role of oxygen vacancies on the performance of $\text{Li}[\text{Ni}_{0.5-x}\text{Mn}_{1.5+x}]\text{O}_4$ ($x = 0, 0.05$ and 0.08) spinel cathodes for Lithium-ion batteries. *Chem. Mater* **24**, 3101–3109 (2012).
19. Yang, J., Han, X., Zhang, X., Cheng, F. & Chen, J. Spinel $\text{LiNi}_{0.5}\text{Mn}_{1.5}\text{O}_4$ cathode for rechargeable lithium ion batteries: nano vs micro, ordered phase (P432) vs disordered phase (Fd3m). *Nano Research* **6**, 679–687 (2013).
20. Liu, J. & Manthiram, A. Understanding the improved electrochemical performances of Fe-substituted 5 V spinel cathode $\text{LiMn}_{1.5}\text{Ni}_{0.5}\text{O}_4$. *J. Phys. Chem. C* **113**, 15073–15079 (2009).
21. Chemelewski, K. R. & Manthiram, A. Origin of site disorder and oxygen nonstoichiometry in $\text{LiMn}_{1.5}\text{Ni}_{0.5-x}\text{M}_x\text{O}_4$ ($M = \text{Cu and Zn}$) cathodes with divalent dopant ions. *J. Phys. Chem. C* **117**, 12465–12471 (2013).
22. Idemoto, Y., Narai, H. & Koura, N. Crystal structure and cathode performance dependence on oxygen content of $\text{LiMn}_{1.5}\text{Ni}_{0.5}\text{O}_4$ as a cathode material for secondary lithium batteries. *J. Power Sources* **119**, 125–129 (2003).
23. Zhang, X. *et al.* Facile polymer-assisted synthesis of $\text{LiNi}_{0.5}\text{Mn}_{1.5}\text{O}_4$ with a hierarchical micro–nano structure and high rate capability. *RSC Advances* **2**, 5669–5675 (2012).
24. Amdouni, N., Zaghbi, K., Gendron, E., Mauer, A. & Julien, C. M. Structure and insertion properties of disordered and ordered $\text{LiNi}_{0.5}\text{Mn}_{1.5}\text{O}_4$ spinels prepared by wet chemistry. *Ionics* **12**, 117–126 (2006).
25. Hai, B., Shukla, A. K., Duncan, H. & Chen, G. The effect of particle surface facets on the kinetic properties of $\text{LiMn}_{1.5}\text{Ni}_{0.5}\text{O}_4$ cathode materials. *J. Mater. Chem. A* **1**, 759–769 (2013).
26. Moorhead-Rosenberg, Z., Shin, D. W., Chemelewski, K. R., Goodenough, J. B. & Manthiram, A. Quantitative determination of Mn^{3+} content in $\text{LiMn}_{1.5}\text{Ni}_{0.5}\text{O}_4$ spinel cathodes by magnetic measurements. *Applied Physics Letters* **100**, 213909 (2012).
27. Santhanam, R. & Rambabu, B. Research progress in high voltage spinel $\text{LiNi}_{0.5}\text{Mn}_{1.5}\text{O}_4$ material. *J. Power Sources* **195**, 5442–5451 (2010).
28. Park, J. S. *et al.* Structurally stabilized $\text{LiNi}_{0.5}\text{Mn}_{1.5}\text{O}_4$ with enhanced electrochemical properties through nitric acid treatment. *J. Power Sources* **230**, 138–142 (2013).
29. Yang, T., Zhang, N., Lang, Y. & Sun, K. Enhanced rate performance of carbon-coated $\text{LiNi}_{0.5}\text{Mn}_{1.5}\text{O}_4$ cathode material for lithium ion batteries. *Electrochimica Acta* **56**, 4058–4064 (2011).
30. Xi, L. J. *et al.* Facile synthesis of porous LiMn_2O_4 spheres as positive electrode for high-power lithium ion batteries. *J. Power Sources* **198**, 251–257 (2012).
31. Fang, H., Wang, Z., Zhang, B., Li, X. & Li, G. High performance $\text{LiNi}_{0.5}\text{Mn}_{1.5}\text{O}_4$ cathode materials synthesized by a combinational annealing method. *Electrochem. Com.* **9**, 1077–1082 (2007).
32. Zhang, D., Popov, B. N. & White, R. E. Electrochemical investigation of $\text{CrO}_{2.65}$ doped LiMn_2O_4 as a cathode material for lithium-ion batteries. *J. Power Sources* **76**, 81–90 (1998).
33. Arrebola, J. C. *et al.* Crystallinity control of a nanostructured $\text{LiNi}_{0.5}\text{Mn}_{1.5}\text{O}_4$ spinel via polymer-assisted synthesis: a method for improving its rate capability and performance in 5 V lithium batteries. *Adv. Funct. Mater* **16**, 1904–1912 (2006).
34. Shaju, K. M. & Bruce, P. G. Nano- $\text{LiNi}_{0.5}\text{Mn}_{1.5}\text{O}_4$ spinel: a high power electrode for Li-ion batteries. *Dalton Transactions* **40**, 5471–5475 (2008).
35. Lee, S., Cho, Y., Song, H. K., Lee, K. T. & Cho, J. Carbon-coated single-crystal LiMn_2O_4 nanoparticle clusters as cathode material for high-energy and high-power Lithium-ion batteries. *Angew. Chem. Int. Ed.* **51**, 8748–8752 (2012).
36. Arrebola, J. C., Caballero, A., Hernan, L. & Morales, J. Expanding the rate capabilities of the $\text{LiNi}_{0.5}\text{Mn}_{1.5}\text{O}_4$ spinel by exploiting the synergistic effect between nano and microparticles. *Electrochem. Solid St. S.* **8**, A641–A645 (2005).

Acknowledgements

We acknowledge the National Natural Science Foundation of China (Grant No. 21273058), China postdoctoral science foundation (Grant No. 2012M520731 and 2014M70350) Heilongjiang postdoctoral financial assistance (LBH-Z12089) for their financial support.

Author Contributions

Y.X., Z.W. and K.K. designed the experiment and wrote the manuscript. L.Z. and F.Y. conducted the experimental parts and carried out data analysis. B.L. and Y.Z. contributed to the characterization processes. All authors reviewed the manuscript.

Additional Information

Supplementary information accompanies this paper at <http://www.nature.com/srep>

Competing financial interests: The authors declare no competing financial interests.

How to cite this article: Xue, Y. *et al.* Investigation on preparation and performance of spinel $\text{LiNi}_{0.5}\text{Mn}_{1.5}\text{O}_4$ with different microstructures for lithium-ion batteries. *Sci. Rep.* **5**, 13299; doi: 10.1038/srep13299 (2015).



This work is licensed under a Creative Commons Attribution 4.0 International License. The images or other third party material in this article are included in the article's Creative Commons license, unless indicated otherwise in the credit line; if the material is not included under the Creative Commons license, users will need to obtain permission from the license holder to reproduce the material. To view a copy of this license, visit <http://creativecommons.org/licenses/by/4.0/>